Energy & Environmental Science

COMMUNICATION

View Article Online
View Journal | View Issue

Cite this: *Energy Environ. Sci.*, 2016, **9**, 2302

Received 31st May 2016,
Accepted 10th June 2016

DOI: 10.1039/c6ee01555g

www.rsc.org/ees

Organic and perovskite solar modules innovated by adhesive top electrode and depth-resolved laser patterning†

George D. Spyropoulos,*[a] César Omar Ramirez Quiroz,[b] Michael Salvador,[bc] Yi Hou,[bd] Nicola Gasparini,[b] Peter Schweizer,[e] Jens Adams,[a] Peter Kubis,[ad] Ning Li,[b] Erdmann Spiecker,[e] Tayebeh Ameri,[b] Hans-Joachim Egelhaaf[a] and Christoph J. Brabec[ab]

We demonstrate an innovative solution-processing fabrication route for organic and perovskite solar modules *via* depth-selective laser patterning of an adhesive top electrode. This yields unprecedented power conversion efficiencies of up to 5.3% and 9.8%, respectively. We employ a PEDOT:PSS–Ag nanowire composite electrode and depth-resolved post-patterning through beforehand laminated devices using ultra-fast laser scribing. This process affords low-loss interconnects of consecutive solar cells while overcoming typical alignment constraints. Our strategy informs a highly simplified and universal approach for solar module fabrication that could be extended to other thin-film photovoltaic technologies.

Broader context

Thin-film photovoltaics using high throughput solution-based printing techniques such as roll-to-roll processing are a key technology for inexpensive and sustainable light-to-energy conversion. Moreover, the use of bendable substrates promotes aesthetically attractive, mechanically amenable and highly customized devices that could advance electronic applications and furnish architectural objects. Here, we demonstrate a micrometer thick PEDOT:PSS–Ag nanowire composite electrode with desirable optical, electrical and adhesive characteristics to establish an entirely solution-processed fabrication route for organic and perovskite solar cells and modules with laminated top electrodes. We employ depth-resolved post-patterning through laminated devices using ultra-fast laser scribing for accomplishing low-loss interconnects of consecutive solar cells thereby overcoming typical alignment constraints. This approach yields geometric fill factors of over 90% and unprecedented power conversion efficiencies of up to 5.3% and 9.8% for organic and perovskite modules with laminated top contact, respectively. Our findings inform materials and engineering strategies for achieving functional devices with integrated barriers and reducing fabrication complexity in future thin-film photovoltaic production lines.

Introduction

As we move through the Information Age, the world faces important challenges resulting from energy demand growth and a rising population. 1.2 billion people or 17% of the world's global population lack access to electricity.[1] Low-cost photovoltaics is one key technology capable of mitigating technological and social inequality. Thin-film organic (OPVs) and hybrid perovskite solar cells are considered promising candidates for sustainable energy production with short energy payback times[2] because they can be processed from solution and deployed on a massive scale while providing excellent form factors[3–5] and competitive power conversion efficiencies.[6–9] Given the prognosis that the cost of a final product based on thin-film photovoltaics is mainly determined by the cost associated with the fabrication and packaging rather than material-related costs,[10] innovation in affordable and reliable large-scale fabrication techniques is imperative.[11]

To fully exploit the economical and engineering advantages with which the roll-to-roll printing technology could benefit an industrial scenario for thin-film photovoltaics, fully solution-processable photoactive and electrode materials are required. Solution-processed metal electrodes are particularly difficult to realize because of often inferior optical (*e.g.*, reflectivity) and electrical properties (*e.g.*, conductivity) as compared to the more common vacuum deposited metal electrodes. Moreover, processing a metal-based electrode from solution on top of a semi-finished stack is challenging in terms of solvent compatibility, surface energy and even surface induced damage. Nevertheless, important advances have been demonstrated lately using for instance silver ink,[12] silver nanowires,[13–15] carbon allotropes[16,17] and hybrid

[a] *ZAE Bayern-Solar Factory of the Future, Energy Campus Nürnberg, Fürthersttraße 250, 90429 Nürnberg, Germany. E-mail: George.Spyropoulos@zae-bayern.de*
[b] *Institute of Materials for Electronics and Energy Technology (i-MEET), Friedrich- Alexander-University Erlangen-Nuremberg, Martensstraße 7, 91058 Erlangen, Germany*
[c] *Instituto de Telecomunicações, Instituto Superior Técnico, Av. Rovisco Pais, P-1049-001 Lisboa, Portugal*
[d] *Erlangen Graduate School in Advanced Optical Technologies (SAOT), Paul-Gordan-Str. 6, 91052 Erlangen, Germany*
[e] *Center of Nanoanalysis and Electron Microscopy (CENEM), Friedrich-Alexander-University Erlangen-Nuremberg, Cauerstraße 6, 91058 Erlangen, Germany*
† Electronic supplementary information (ESI) available. See DOI: 10.1039/c6ee01555g

electrodes, *e.g.*, conductive polymer/metal grids,[18,19] without significantly sacrificing the efficiency.

An alternative concept for the realization of high-quality electrodes in a low-cost, large-area compatible fashion is roll lamination. In general, a transparent, conductive film with adhesion properties (TCA; transparent conducting adhesive) is coated onto a substrate and is activated by applying temperature and/or pressure. The TCA provides electrical and mechanical functionality compatible with the requirement of bendable devices. Roll lamination is particularly attractive because it allows decoupling of the processing of the top electrode from the rest of the device fabrication procedure. This could greatly simplify a production line, for instance, by allowing switching between the fabrication of single and tandem solar cells, the latter *via* post-connection of two sub-cells. Furthermore, the substrate of the laminated top electrode could function as a barrier for environmental contaminants and thus enable encapsulation at the earliest possible fabrication stage.

Previous work has focused on demonstrating lamination as a potentially simple fabrication route for bilayer structures,[20,21] organic light-emitting diodes,[22] semi-transparent organic solar cells[23] and metal electrodes in general.[24–26] In this context, a conductive adhesive consisting of PEDOT:PSS and sorbitol has proven to be particularly effective, but other conductive glues have been explored as well.[27–32] Organic solar cells produced using this method have shown power conversion efficiencies of up to 4% (Table S1, ESI†). More recently, alternative materials and lamination techniques to produce single or tandem organic and perovskite solar cells were presented.[33–36]

While previous results are indicative of the future potential of lamination technology, at present the implementation of this technology as an efficient method for producing up-scalable electrodes and devices hinges on several hurdles. First, thick electrode materials (micron range) that efficiently extract charge carriers upon being coated using simplified solution-based methods are not easily accessible. The main challenges associated with the realization of such a functional electrode are often limited by the trade-off between the adhesion and the electrical properties as well as by the quality of the contact between the TCA and the active layer on one side and the TCA and the current collection electrode on the other side. Additionally, a proof of concept by transferring this technology to a solar module that delivers tunable voltage output is needed to demonstrate the feasibility and applicability of the concept. Importantly, the fabrication of a module using a laminated electrode bears several key challenges associated with the realization of an efficient electrical connection between two successive cells (P2 line) and the separation of the top electrode (P3 line) for defining electric current pathways, in both cases without sacrificing the active area. Specifically, high performance devices call for a top electrode that fills the P2 area and forms an ohmic contact with the bottom electrode upon lamination (Fig. 1). Furthermore, a second important challenge lies in aligning the P3 line relative to the P2 line when laminating the electrode on top of the active layer (Fig. 1). This may induce major photocurrent losses because the standard procedure requires the typically pre-patterned P3 line to be wide enough so that the electrical separation is not jeopardised upon lamination, which necessarily translates into a loss of photoactive area (dead area).

Here, we report on a roll lamination process to demonstrate fully solution-processed, laminated organic solar modules with 5.3% power conversion efficiency. This was accomplished by the development of a highly functional adhesive electrode consisting of embedded silver nanowires and a transparent conductive adhesive (TCA). The latter is based on a blend of highly conductive PEDOT:PSS and D-sorbitol. We confirm the optoelectrical quality of this laminated top electrode using full-frame dark lock-in thermography (DLIT), impedance spectroscopy (IS) and capacitance *versus* voltage measurements (C^{-2}–V). A key innovation of the flexible modules with laminated top electrode is depth-resolved post-laser patterning using a pulsed femtosecond laser. The laser beam penetrates the top substrate after the lamination process and ablates the composite electrode beneath without damaging the top plastic substrate. This step eliminates common alignment constraints of traditional module coating and allows for large geometrical fill factors (>90%). We further confirm the general application of this concept by fabricating laminated perovskite solar cells and modules with 9.80% and 9.75% efficiency, respectively. We thus anticipate that the adhesive AgNW:PEDOT composite electrode by itself or combined with depth-resolved laser patterning is likely to be compatible with and of benefit to many thin film photovoltaic technologies.

Materials and methods

Materials

PBTZT-stat-BDTT-8 was provided by Merck Company (Fig. S1, ESI†). Phenyl-C61-butyric acid methyl ester [60]PCBM (99%) was obtained from Solenne BV. ZnO nanoparticles dispersed in isopropanol (Product N-10) was received from Nanograde AG. PEDOT:PSS (Clevios™ PH 1000) and D-sorbitol were acquired from Heraeus and Sigma-Aldrich, respectively. Silver nanowires (AgNWs) dispersion (ClearOhm ink) was purchased from Cambrios Technologies Corporation. Polyethylene terephthalate PET (Melinex® DuPont Tejin) and indium tin oxide–Ag–indium tin oxide IMI-based flexible PET foils were purchased from Pütz-Folien and Materion, respectively. Indium tin oxide (ITO) coated glass was obtained from OSRAM. Branched PEI solution (50 wt% in H_2O) was purchased from Sigma-Aldrich. Dry NiO nanopowder was prepared by flame spray synthesis using a precursor solution of nickel acetate in 2-ethylhexanoic acid; the solution was diluted using 30 wt% xylene. The precursor was then fed (7 ml min^{-1}) into a spray nozzle, dispersed by oxygen (9 l min^{-1}) and ignited by a premixed methane–oxygen flame (CH_4: 1.2 l min^{-1}, O_2: 2.2 l min^{-1}). The off-gas was filtered through a steel mesh filter (20 micron mesh size) using a vacuum pump at about 20 m^3 h^{-1}. The obtained NiO nanopowder was collected from the filter mesh. A stable suspension was prepared by dispersing 5 wt% NiO nanopowder in methanol by using an undisclosed dispersant (proprietary information of Nanograde Ltd). PbI_2 and CH_3NH_3I powders were purchased from Sigma-Aldrich and

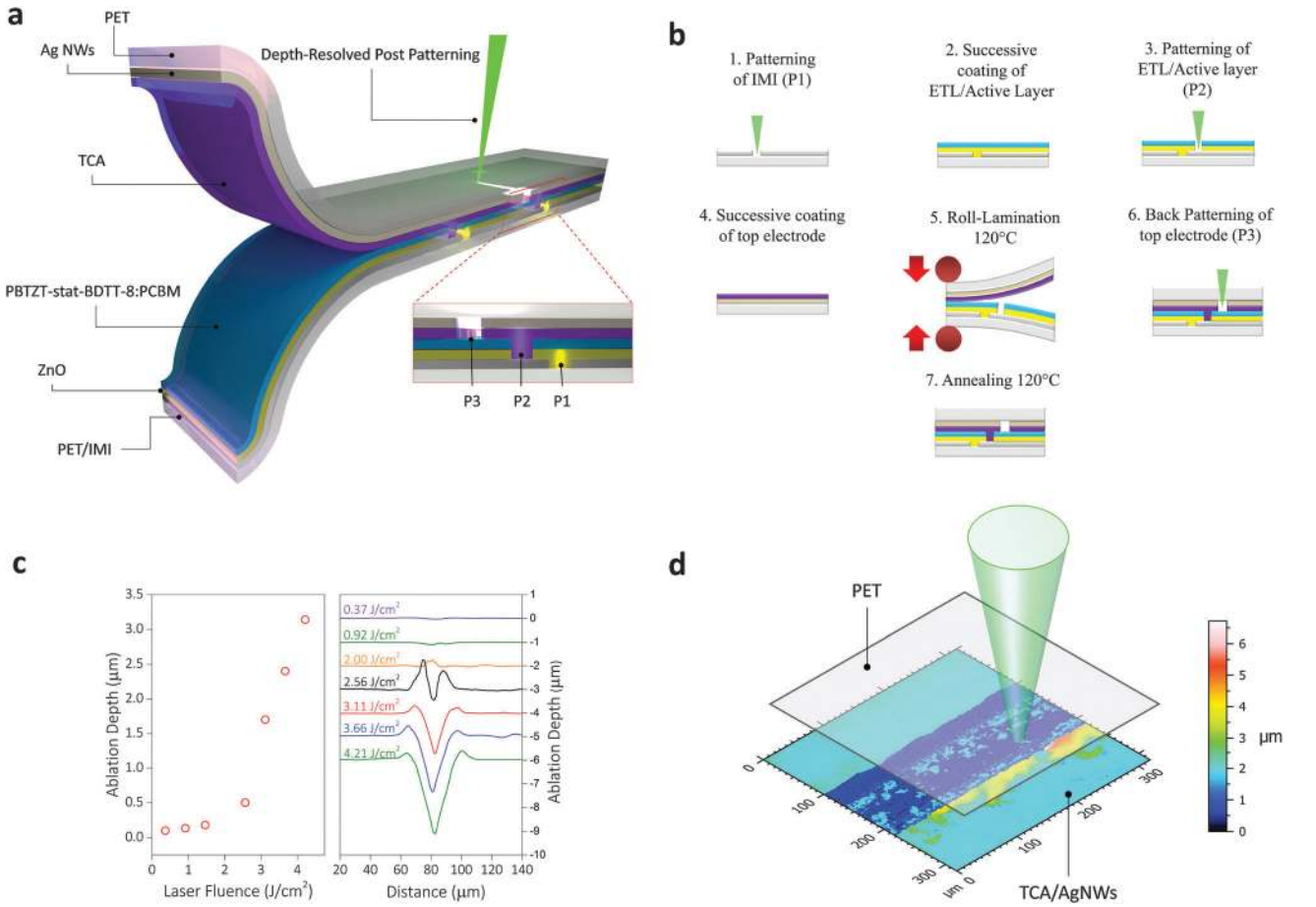

Fig. 1 (a) Architecture of laminated organic solar cell/module and illustration of depth-resolved post-patterning of the top electrode (P3) using a femtosecond laser. Inset shows laser-patterned lines required for the interconnection of successive cells, *i.e.* module fabrication. (b) Step-wise fabrication route of solution-processed roll laminated modules. ETL: electron transporting layer, IMI: ITO/Ag/ITO. (c) (left) Ablation depth upon laser patterning of adhesive top electrode *versus* the laser fluence applied. (right) Representative ablation depth profiles for different laser fluences as determined from confocal optical microscopy images. (d) Schematic representation of post-laser ablation of a P3 line through a PET foil after lamination and the corresponding 3D depth profile.

Dyenamo, respectively. All anhydrous solvents were acquired from Sigma-Aldrich.

Laminated organic solar cell fabrication

All layers were coated by doctor blading in an ambient environment. The final structure of our solar cells is depicted in Fig. 1a. Excluding the steps 3 and 6, Fig. 1b illustrates the fabrication route of laminated solar cells. IMI-based PET was cleaned with isopropanol (IPA). Subsequently, the substrates were coated with a ≈30 nm ZnO layer and dried on a hotplate at 80 °C for 5 minutes, on top of which an active layer of ≈300 nm was deposited by coating a solution of PBTZT-stat-BDTT-8:[60]PCBM (1 : 2 wt%, 32 mg ml^{-1} in total). The solution was based on a mixture of solvents: xylene : tetrahydronaphthalene (9 : 1). In parallel, the top electrode of the device was prepared by coating an approximately 100 nm thick Ag NW layer on a clean PET substrate that was dried for 3 minutes at 100 °C. To conclude the electrode, a conductive glue based on a mixture of PEDOT:PSS (Clevios™ PH 1000) and D-sorbitol (40% w/w) was coated on top of the AgNW layer and the stack was placed again on a hotplate for 3 minutes at 100 °C. Finally, we laminated our devices by passing the sandwich structure through a pre-heated (120 °C) roll laminator (Fig. S2, ESI†). The obtained device was annealed for 10 minutes at 120 °C. Solar cells with a 100 nm thick evaporated Ag electrode were prepared similarly but with a thin ≈50 nm PEDOT:PSS (Clevios P VP Al408) layer immediately coated on top of the active layer.

Laminated perovskite solar cell fabrication

Cleaned ITO-coated glass substrates were coated with a NiO layer (Fig. S3, ESI†) at a speed of 4000 rpm and annealed for 10 minutes at 140 °C in air. The DMF-perovskite precursor was prepared by adding PbI_2 and CH_3NH_3I powders in a molar ratio of 1 : 1 and a concentration of 40 wt% and 20 wt%, respectively, to a vial and mixed with anhydrous dimethylformamide (DMF). The solution was then stirred for 30 minutes at 60 °C and filtered through a 0.45 µm PTFE syringe filter prior to deposition. The precursor solution was spin coated inside a glovebox at room temperature at a rotation speed of 4000 rpm for 35 seconds. During the last 5 seconds of the spinning process, the layer was

treated with drop-cast chlorobenzene solution. The substrate was dried on a hotplate for 10 min at 100 °C. After depositing the perovskite solution, a compact 60 nm thick layer of [60]PCBM was spin coated on top. The 2 wt% solution of [60]PCBM in chlorobenzene was deposited using a three-step speed profile with no subsequent annealing. The ZnO film was spin coated at 2000 rpm and annealed for 5 minutes at 80 °C. PEI was spin coated at 1000 rpm and annealed for 5 minutes at 80 °C. In this case, the top electrode was pressure laminated at 60 °C inside a glovebox. Solar cells with an electrode consisting of 100 nm of evaporated Ag were prepared in the same way.

Laminated module fabrication

Fig. 1b illustrates the complete fabrication route for laminated modules. The laser patterning was carried out using a LS – 7xxP laser patterning setup built by LS Laser Systems (München, Germany), consisting of an ultrafast laser femtoREGEN^{TM} UC – 1040–8000 fs Yb SHG from High Q Laser (Rankweil, Austria)[39] and a beam guiding system (4 mirrors and a galvanometer scanner). The scanner's objective has a focal length of 330 mm and a focal spot diameter of 32 ± 2 μm (at $1/e^2$ intensity). The alignment of the laser beam was realized using a CCD camera and the software positioning system developed by LS Laser Systems. The power of the laser was measured using the VEGA DISPLAY and a 30A-BB-SH-18 ROHS sensor from Ophir Optronics (Jerusalem, Israel). The laser patterning of the IMI (P1 line) was accomplished with a laser fluence of 0.25 J cm^{-2} and an overlap of 50%. The P2 line in the active layer was patterned before the lamination process with a laser fluence of 0.085 J cm^{-2} and an overlap of 94%. Finally, the laser patterning of the AgNWs/TCA electrode (P3 line) was performed by controlled depth selective ablation through the top PET layer. All lines were scribed with a 520 nm laser wavelength (Fig. S4 and S5, ESI†).

Characterization

The area of the photovoltaic devices investigated in this work was defined by the patterning layout of the bottom electrode and confirmed through optical microscopy. The *J–V* characteristics were measured using a source measurement unit from BoTest. Illumination was provided by a solar simulator (Oriel Sol 1A, from Newport) using an AM 1.5G spectrum at 100 mW cm^{-2}. To exclude contributions outside the active area, we measured the *J–V* characteristics using an aperture masking out the active area. In the case of perovskite-based devices, *J–V* characterization was carried out as follows: forward direction, speed: 1 mV ms^{-1} and a dwell time of 8 ms. The measurements of hysteresis and stability effects are shown in Fig. S6 (ESI†). External quantum efficiency (EQE) measurements were carried out using a QE-R system from Enlitech. Dark lock-in thermography (DLIT) measurements were carried out using an EQUUS 327k NM IR camera system (IRCAM GmbH, Erlangen, Germany), equipped with an indium antimonite (InSb) and focal plane array detector providing a spatial resolution of 640 × 512 pixels. The IR-camera was controlled by a computer to guarantee a real-time lock-in calculation of the measured IR signal. The InSb detector is highly responsive in a spectral range between 1.5 μm and 5 μm with a noise equivalent temperature difference less than 20 mK and a frame rate of 100 Hz. For focusing, a 25 mm focal lens imaging system providing a spectral transparency >90% (IRCAM GmbH, Erlangen, Germany) was used. The lock-in frequency was set to 10 Hz in order to minimize implications due to the heat diffusion length. Each test sample was excited for 120 s using a pulsed injection current of 3.5 mA. As a power supply for the pulsed excitation, a source measure unit from Agilent (B2900) in combination with a switch circuit was used. Impedance spectroscopy measurements were conducted using an Agilent HP 4192A impedance analyzer. For acquiring Nyquist plots the impedance spectra were taken in the dark by superimposing a harmonic voltage modulation (ac amplitude of 20 mV), with frequencies ranging from 10 Hz to 1 MHz, and different dc biases. The *C–V* measurements were taken in the dark at a frequency of 10 Hz.

A FEI Helios Nanolab 660 was used to prepare cross-sections of the solar cells using focused ion beam (FIB) milling as well as to acquire scanning electron microscopy (SEM) images of those cross-sections. Before FIB milling the devices were delaminated to expose the layer stack. For the FIB milling, gallium ions accelerated at 30 kV were used with a final current of 80 pA. Before milling a carbon layer was deposited to protect the area of interest using beam induced deposition (first 50 nm electron beam induced, then ion beam induced). The SEM images were taken with an acceleration voltage of 2 kV at an electron current of 100 pA. Bending tests were performed on a bending drum with a diameter of 28 mm.

Results and discussion

Laminated solar cells

First, we fabricated a flexible photovoltaic device with a laminated top electrode by adopting a solution process that is based on doctor blade coating in air (Fig. 1a). A mechanically robust IMI (ITO/Ag/ITO) coated PET foil featuring a sheet resistance of 7.7 Ω sq^{-1} was chosen as the transparent bottom electrode.[37] On top of IMI, we processed commercial ZnO nanoparticles (Nanograde) as the electron selective electrode. As a photoactive layer we coated a medium band gap conjugated polymer PBTZT-stat-BDTT-8[38,39] (Fig. S1, ESI†) blended with phenyl-C61-butyric acid methyl ester [60]PCBM on top of ZnO (see Materials and methods for details). The active layer was contacted with a laminated electrode that was prepared in a separate step.

In contrast to previous work, where primarily the combination of a transparent conductive adhesive with sputtered electrodes[23] and evaporated[30] or complex mesh structures[29,31] has been explored, the laminated electrode designed in this work consists of a bilayer of successively coated TCA and AgNWs on a PET foil (Fig. 1b). As a TCA we optimized a mixture of highly conductive PEDOT:PSS (~850 S cm^{-1}) and D-sorbitol.[23] The highly conductive PEDOT:PSS ensures sufficient electrical connection between the active layer and the AgNWs, while D-sorbitol provides the necessary adhesive force for establishing a robust connection between the two substrates. Significantly, the combination of TCA with AgNWs affords process simplicity, semi-transparency and high-quality electrical contacts. AgNWs are easily coated

from a water-based solution, requiring only a simple and short drying process at 100 °C for 3 min. Aside from the ease of processing, AgNWs are known to form macroscopic mesh electrodes (Fig. 2b) with low sheet resistance (10 Ω sq^{-1}) and average optical transmittance of better than 70% (Fig. 3a). Notably, we found a good ohmic contact with the conductive adhesive, enabling charge carrier extraction similar to evaporated silver, as discussed later on. Importantly, the AgNW electrode is compatible with the technical requirements of many photovoltaic technologies and can be easily exported to, *e.g.*, CIGS (copper indium gallium selenide solar cells) or a-Si:H (amorphous silicon) solar cells, facilitating the implementation of the hybrid tandem technology. Fig. 2a depicts a macroscopic cross-sectional scanning electron micrograph of a device with laminated top electrode. It is apparent that the TCA (~2 μm) is substantially thicker than the active layer (280–290 nm). The overall thickness of the TCA is the result of the combination of optimized coating of the glue, applied pressure and resulting adhesion. We further note that polymer blend layers featuring PBTZT-stat-BDTT-8 can be coated as thick as 500 nm without significant roll off in photovoltaic performance.[38]

Solar modules by depth-resolved laser patterning

Our proposed fabrication route for the realization of solar modules with laminated top electrode involves an innovative depth-resolved post-patterning technique (Fig. 1b). The fabrication is fully roll-to-roll compatible due to the high processing speed of our laser patterning approach (up to 4 m s^{-1}) and solution processing of all functional layers under ambient conditions. The device fabrication consists of seven consecutive coating, lamination and patterning steps. Generally, in order to achieve electrical series interconnection between individual cells in a solar module, three patterning lines P1–P3 are necessary (Fig. 1a, inset, and Fig. S4, ESI†). We utilize femtosecond–laser patterning with optimized ablation thresholds (Fig. S5, ESI†) for each interconnection line

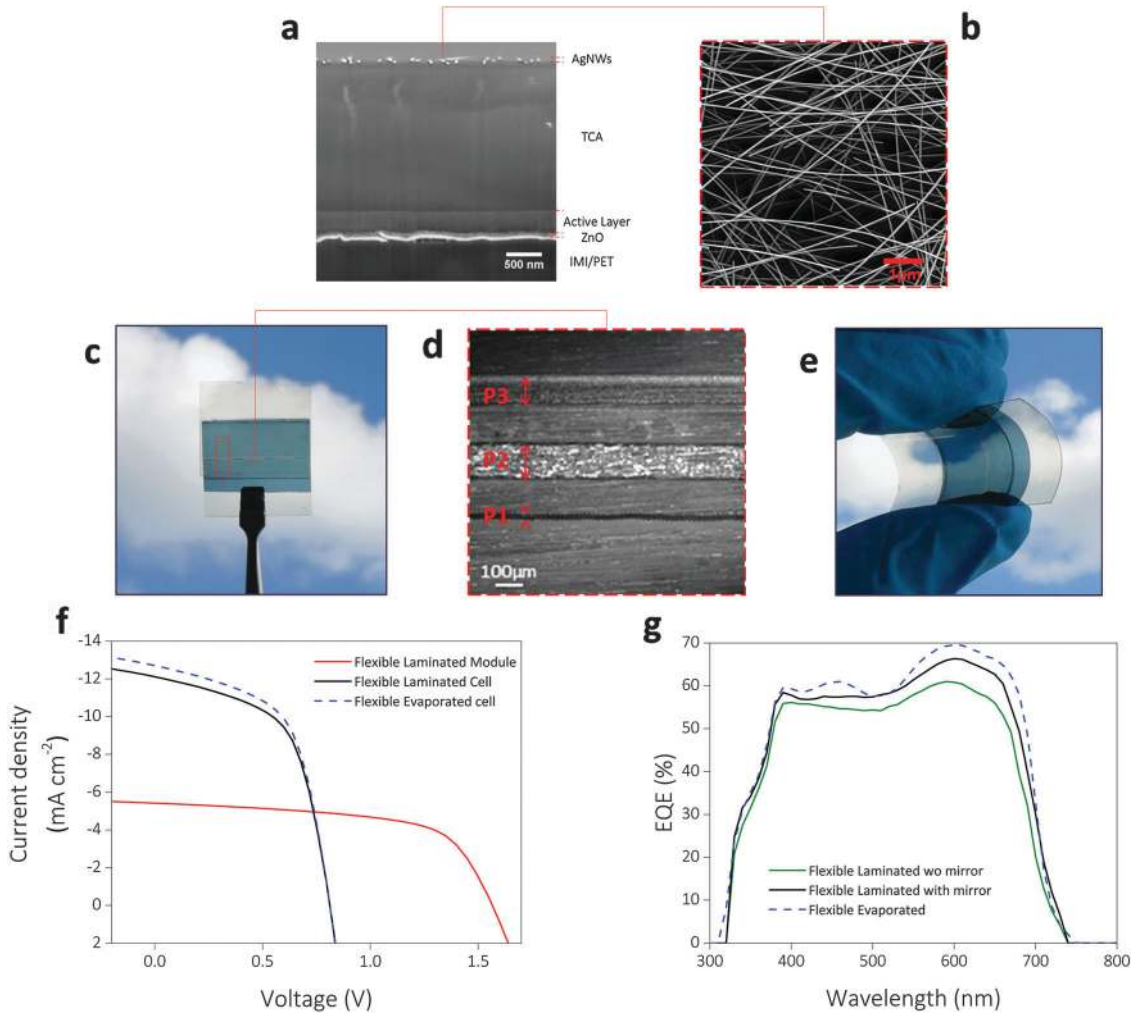

Fig. 2 (a) Cross-section scanning electron microscopy (SEM) image of the flexible laminated organic solar device. (b) Top view of AgNWs on TCA after delamination of the PET substrate. (c) Photograph of a substrate with three laminated modules (2-cell module) in a relaxed state. The red rectangle highlights one module. (d) Optical microscope image displaying the laser patterning lines P1–P3 taken through top PET. (e) Photograph of a bent module. (f) Current–voltage (*J*–*V*) characteristics of organic solar cells and modules with laminated top electrode. (g) EQE spectra of reference OPV solar cell with evaporated silver top electrode (100 nm, blue dashed line), laminated OPV solar cell with reflecting mirror in the back (black line), and laminated OPV solar cell measured without reflecting mirror (green line).

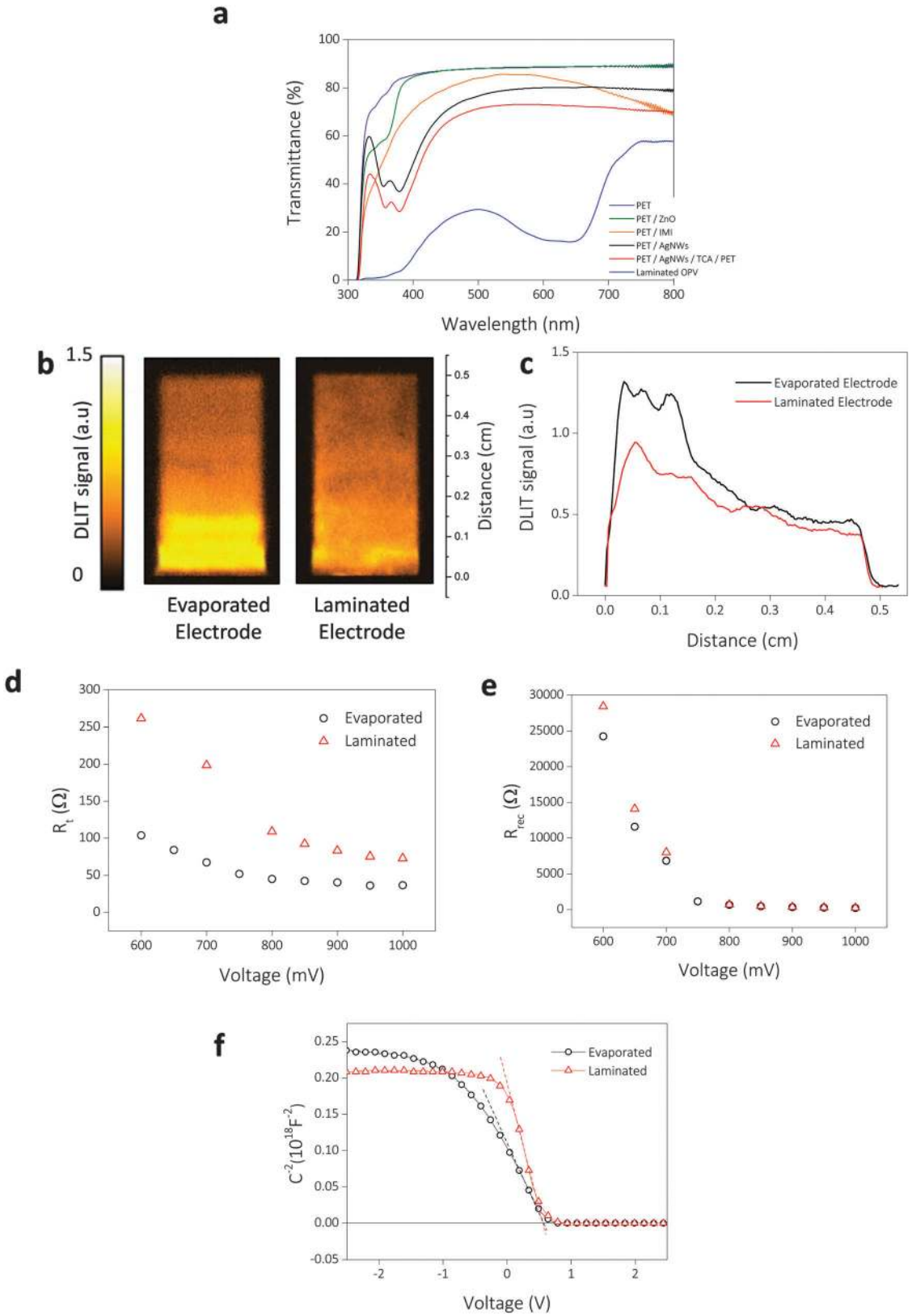

Fig. 3 (a) Transmittance spectra of PET substrate, charge extraction layers, laminated electrode and a full device. (b) DLIT images of solar cells with evaporated and laminated top electrode. The *y*-axis on the right depicts the distance from the edge of the active area of the solar cell. (c) Integrated DLIT signal profile along the long axis of the DLIT image. The *x*-axis refers to the distance from the edge of the active area, in analogy to (b). (d) Transport resistance R_t and (e) recombination resistance R_{rec} as a function of applied bias for devices with evaporated and laminated electrodes. (f) Mott–Schottky plot (10 Hz) for devices with evaporated and laminated top electrodes. The dashed lines represent linear fits to the slope. A scheme of the equivalent electrical circuit model used for analyzing impedance spectroscopy data is displayed in Fig. S8 (ESI†).

to take advantage of high spatial resolution and low geometrical fill factor (GFF, the ratio between the photoactive area and the total area of the module) losses.

The advantages and challenges associated with laser patterning of thin-film solar modules have been elucidated before.[40] Typically, a laser source irradiates the active layer material of a device with ultra-short laser pulses, inducing a phase transition from solid to vapor. The minimum energy required for this phase transition is an intrinsic material property and known as the ablation threshold. Given the differences in the ablation threshold for the electrode, interface and photoactive materials chosen here (reported in Fig. S5, ESI†) and by tuning the laser fluence, we can ablate functional layers of a device individually. More importantly, we demonstrate that the controlled ablation of functional layers is even feasible through a plastic barrier, *i.e.*, upon lamination of the top electrode, extending the concept of laser patterning to depth-resolved laser patterning. This allows effectuating the last patterning step upon protecting the susceptible device structure from environmental contaminants.

We now turn to the laser patterning steps for module fabrication based on laminated devices. Following laser structuring of the bottom IMI electrode (P1 line) for defining the sub-cells of the module (Fig. 1b), the electron extraction ZnO layer and photoactive layer are successively coated. During the third step of the module fabrication the active and ZnO layers are ablated to form the P2 line. This requires a laser fluence smaller than the ablation threshold of the bottom electrode (Fig. S5, ESI†). It is critically important that the P2 line is free of residuals and debris as this is the area that will later determine the quality of the electrical interconnection (between the top and successive bottom electrodes). In a separate process, the TCA and AgNWs are consecutively coated onto a different substrate to form the top electrode, which is simply assembled on top of the active layer by passing through a pre-heated (120 °C) roll-laminator (pressure $\sim$2 bar, Fig. S2, ESI†). The final patterning of the top electrode is then performed through the plastic substrate using depth-resolved laser structuring. We emphasize that the laser fluence can be fine-tuned such that the TCA/AgNWs electrode is selectively ablated, without notably damaging either the top PET substrate or the bottom electrode. The depth selectivity of this process is demonstrated by plotting the ablation depth as a function of the laser fluence (Fig. 1c, left) as well as the corresponding depth profiles (Fig. 1c, right). The latter was extracted from confocal microscopy images upon laser structuring of the TCA/AgNWs layer (Fig. 1d). We observe that after a relatively slow increase of the ablation depth with increasing laser fluence the depth increases rapidly after $\sim$2.5 J cm^{-2}. We associate the slow initial increase with the melting and consecutive ablation of the top AgNWs film, while the steeper slope is likely related to the removal of the TCA. A $\sim$2 μm thick TCA layer can be fully ablated at a laser fluence of $\sim$3 J cm^{-2}. While this laser fluence exceeds the threshold fluence for the bottom IMI (Fig. S5, ESI†), the 2 μm thick TCA acts as a buffer layer and protects the rest of the device from potential damage. Fig. 1d shows the topography of a representative P3 line as obtained using a confocal microscope after delaminating the top PET substrate. We note that even though throughout the ablation of the TCA the laser beam may penetrate and thus dissipate part of the photovoltaic blend layer, this does not affect device performance as the ablation occurs within the dead area, which does not contribute to the photocurrent of the device. Instead, the main concern for the dead area when scribing the P3 line is to preserve the electrical pathway by not destroying the bottom electrode.

Based on the above results, it is clear that the combination of lamination and depth-resolved laser patterning is particularly attractive because it alleviates both typical constraints in fabricating thin-film devices from solution as well as active area losses. Furthermore, the top substrate may simultaneously act as a barrier. In a large-scale fabrication line this procedure would allow environmental protection of the sensitive active layer at an early fabrication stage. Simultaneously, this method reduces fabrication complexity as the adjustment of the P3 line with respect to the P2 and P1 lines can be well controlled with the laser and obviates mechanical alignment of the substrates. Importantly, the introduction of depth selective laser scribing constitutes the first step towards a post-patterning technology in which all patterning lines (P1, P2 and P3) can be scribed by depth-resolved laser patterning. The latter would be applied as the very last device fabrication step upon uniform full-area coating of all functional layers. Finally, the integration of such a fabrication route in a future solar factory would allow not only for a continuous production line of inexpensive, semi-transparent and flexible solar modules, but also, more generally, for post-connection of two parallel production lines into a tandem or multilayer concept.

Performance and key characteristics of laminated devices

Fig. 2 displays scanning electron and optical micrographs as well as photographs of roll-laminated photovoltaic devices under relaxed and bent conditions. A cross-sectional scanning electron microscopy (SEM) image (Fig. 2a) of a completed device visualizes the uniformly coated active and charge extraction layers on top of a PET/IMI substrate. The $\approx$2 μm thick TCA takes up most of the device thickness. The AgNWs are apparent as bright spots in the upper part of the SEM cross-section. A top-view SEM reveals the typical random mesh configuration (Fig. 2b). The *J*–*V* characteristics of flexible OPV solar cells and modules under 1000 W m^{-2} solar simulator light are shown in Fig. 2f. In agreement with the common procedure in the literature, all devices with laminated electrode were measured with a reflecting mirror placed in the back. Optimized solar cells with laminated top electrode deliver an open circuit voltage (V_{oc}) of 810 mV, a short circuit current density (J_{sc}) of 12.10 mA cm^{-2} and a fill factor (FF) of $\approx$59%. This corresponds to a power conversion efficiency of 5.9%. Comparison between OPV devices with laminated and evaporated silver electrode (the latter consisting of IMI/ZnO/PBTZT-stat-BDTT-8:[60]PCBM/PEDOT:PSS($\approx$50 nm)/Ag, evap.) reveals that the losses in PCE are mainly dominated by J_{sc} losses ($\approx$5%), which is in good agreement with the integrated photocurrent from the corresponding EQE spectra (Fig. 2g and Table S2, ESI†). The difference in J_{sc} is likely to be associated with differences in electromagnetic

Table 1 Key metrics for organic and perovskites solar devices with evaporated and laminated top electrode under AM 1.5G illumination (100 mW cm^{-2}). Best performance and mean values with standard deviation population (shown in parenthesis) were extracted from 10 organic devices and 5 perovskite devices. The corresponding J_{sc} values as calculated from EQE spectra are shown in Table S2 (ESI)

	Top electrode	V_{oc} (V)	J_{sc} (mA cm^{-2})	FF (%)	PCE (%)	Device area (mm^2)
PBTZT-stat-BDTT-8:PCBM cell	Evaporated Ag	0.81 (0.80 ± 0.01)	12.70 (12.40 ± 0.18)	60.05 (59.10 ± 0.84)	6.19 (5.87 ± 0.18)	15
PBTZT-stat-BDTT-8:PCBM cell	Laminated	0.81 (0.81 ± 0.01)	12.10 (11.78 ± 0.28)	59.24 (59.16 ± 0.57)	5.88 (5.65 ± 0.13)	15
PBTZT-stat-BDTT-8:PCBM module	Laminated	1.57 (1.57 ± 0.01)	5.42 (5.38 ± 0.06)	62.31 (60.56 ± 1.28)	5.33 (5.15 ± 0.15)	30
$CH_3NH_3PbI_3$ cell	Evaporated Ag	1.04 (1.06 ± 0.02)	18.53 (18.05 ± 0.38)	70.35 (68.09 ± 1.72)	13.56 (13.10 ± 0.32)	15
$CH_3NH_3PbI_3$ cell	Laminated	1.01 (1.03 ± 0.02)	16.44 (16.05 ± 0.56)	59.54 (56.61 ± 1.95)	9.80 (9.36 ± 0.40)	15
$CH_3NH_3PbI_3$ module	Laminated	2.00 (2.00 ± 0.01)	8.12 (7.90 ± 0.22)	60.00 (57.54 ± 1.60)	9.75 (9.10 ± 0.34)	30

field distribution and the resulting interference profile. Remarkably, we demonstrate OPV modules (two in series connected solar cells) with laminated top electrode that exhibit a champion efficiency of 5.3% and thus only minor losses in PCE (≈10%) as compared to reference solar cells. These losses are predominantly determined by the J_{sc} value, which is only ≈10% lower than the maximum limit for in-series connected modules (current corresponding to half of the reference cell), and can be attributed to the GFF. The GFF was found to be ~91% (considering the sum of active and dead areas and neglecting possible bus bar losses).[37] The V_{oc} losses are restrained to ~3% with respect to the maximum V_{oc} of a two-cell module. With 62% the FF is even slightly higher than that in the reference cell, confirming the quality of the active layer and interfaces in the module. The reported mean values and standard deviation population values of the laminated devices confirm good reproducibility (Table 1). The *J–V* characteristics in the dark are shown in Fig. S7a (ESI†).

Optoelectrical performance of the adhesive top electrode

It is intriguing that such a thick polymer/adhesive/AgNW-based laminated electrode as the one shown in Fig. 2a allows efficient photovoltaic module performance. In the following we analyze the optical and electrical properties of the laminated composite electrode. Fig. 3a shows the typical transmission spectra of the laminated electrode, the PET substrate and the relevant charge extraction layers. The transmission spectrum of the TCA electrode shows the characteristic localized surface plasmon resonance of AgNWs of around 380 nm and an average transmission of ≈70% between 400 nm and 800 nm. The final OPV devices with adhesive top electrode and an active layer of 290 nm show an average transmittance of ≈31% for the same wavelength range. To investigate the electrical characteristics and homogeneity of the laminated electrode we applied impedance spectroscopy and dark lock-in thermography (DLIT). DLIT is a sensitive full-frame infrared imaging technique that reveals local thermal loss processes.[41] Fig. 3b compares two devices with laminated and evaporated top electrodes but with otherwise identical layer stacks. For DLIT measurements, the devices were operated under 1 V forward bias (charge carrier injection regime). Both electrodes show a typical temperature gradient behavior with higher temperatures closer to where the IMI electrode was contacted (Fig. 3b and c). This observation originates from the difference in sheet resistance between the bottom electrode (IMI) and the top electrode of the solar cell (evaporated or laminated).[41,42] The laminated electrode reveals a DLIT image with similar temperature profile gradient and homogeneity to the device with evaporated silver, suggesting a homogenous and fully functional electrode with no major irregularities in current transport across the IMI and laminated Ag NW electrodes. In order to further investigate the effect of the laminated electrode on the device behavior, we conducted AC impedance spectroscopy and capacitance *versus* voltage measurements.[43–45] The Nyquist plots in the dark for varied applied biases are represented in Fig. S8a and b (ESI†). Similar to previous reports on OPV devices, the data are best fitted using an equivalent circuit model that includes two resistor–capacitor sub-circuits and an additional resistive element due to electrode resistance losses (Fig. S8c, ESI†), which accounts for the total resistance in the device.[43,44] Using this model, we extract the resistance elements of our devices over the range of different applied bias. It has been previously established that the high-frequency impedance response is primarily related to the transport resistance (R_t) of photo-generated carriers being extracted at the contacts while the low-frequency response can be associated with recombination resistances in the bulk (R_{rec}).[43,44] Qualitatively, for optimum device performance R_{rec} should be large and R_t should be small for voltages corresponding to the fourth quadrant of the *J–V* graph. The recombination resistance of devices with evaporated electrode is almost identical to the ones with laminated electrode as demonstrated by the similar exponential decay with applied bias (Fig. 3e). Minor variations in the regime $V < V_{oc}$ may reflect small variations in device thickness or in the electrical field distribution. This is not surprising considering the usage of the same photoactive blend. For voltages greater than V_{oc} the recombination resistance approaches zero in both cases, reflecting the higher probability for the generated carriers to vanish through bimolecular recombination. Conversely, a comparison between the transport resistances (R_t) shows values of similar order of magnitude (two orders of magnitude lower than R_{rec}) but higher order of magnitude over the whole scan of voltages for the device with a laminated top electrode (Fig. 3d). The larger R_t is representative of higher contact resistance of the laminated electrode and probably further dominated by the thickness of the TCA in the laminated devices. Since the probability for charge extraction depends on the correlation between R_{rec} and R_t,[46] the observation of comparatively low R_t, even in the case of laminated devices, grants efficient carrier extraction in both cases and thus comparable device performance.

Mott–Schottky (C–V) measurements can reveal important insight regarding the quality of the electrode and electrode-bulk interface[45] (Fig. 3f), particularly when comparing laminated and evaporated electrodes. By fitting a straight line to the region of C^{-2} *vs.* V with the steepest slope it is possible to extract the built-in potential (V_{bi}).[45] Importantly, both devices demonstrate similar values of V_{bi} ($\sim$0.57 V), which evidences qualitatively similar energetic offsets at the electrode-bulk interface. In addition, in the high reverse bias regime ($V \ll V_{bi}$) both samples show dielectric capacitor behavior, approaching a constant capacitance that corresponds to the geometrical capacitance.[45] In the forward bias regime ($V > V_{bi}$), the capacitance is mainly determined by the chemical capacitance.[45] Different Mott–Schottky behaviors under low reverse and forward biases ($V < V_{bi}$) are observed. For devices with evaporated electrode the capacitance starts to increase at more negative voltages, denoting an early starting point of a more gradual decrease of the depletion width and high doping density, $N = 1.04 \times 10^{16}$ cm^{-3}. The latter is determined from the corresponding slopes by $N = -2(\mathrm{d}C(x)^{-2}/\mathrm{d}V)^{-1}/q\varepsilon_0\varepsilon_r A^2$, where q denotes elementary charge, ε_0 = dielectric constant of vacuum, and ε_r = dielectric constant of the semiconductor (assumed value of 3.5).[47] In contrast, laminated devices show an inclination point at a relatively low reverse (more positive) bias, revealing a faster depletion zone collapse over the voltage scan and a lower doping density $N = 5.09 \times 10^{15}$ cm^{-3}. The higher doping density for devices with evaporated electrode may arise due to the diffusion of small molecules such as oxygen and water migration or evaporated "hot" silver atoms into the photoactive layer.[48–50] These phenomena have been reported before and in the case of oxygen and water, they could be even propelled due to the intimate contact of the active layer with a wet, water based PEDOT:PSS solution during device fabrication. For laminated electrode devices, the TCA was coated onto a different substrate and applied on top of the active layer after a drying step. The difference in doping density highlights the possible advantage of the procedure, in which electrodes or additional layers are processed on different substrates and assembled afterwards.

In order to characterize the performance of our devices as a function of mechanical stress, we performed bending tests on a drum with 28 mm radius (Fig. S9, ESI†). We reinforced the edges of the devices using a commercial adhesive tape (Scotch™ tape). After 1000 bending cycles the performance decreases to $\sim$59% of the initial value, mainly due to J_{sc} and FF losses. This suggests that the main cause for the mechanically induced performance roll-off is the damage caused to the interface between the active layer and the adhesive electrode.

The above-mentioned properties grant tremendous inherent advantages to the laminated electrode: low temperature ($\leq$120 °C),

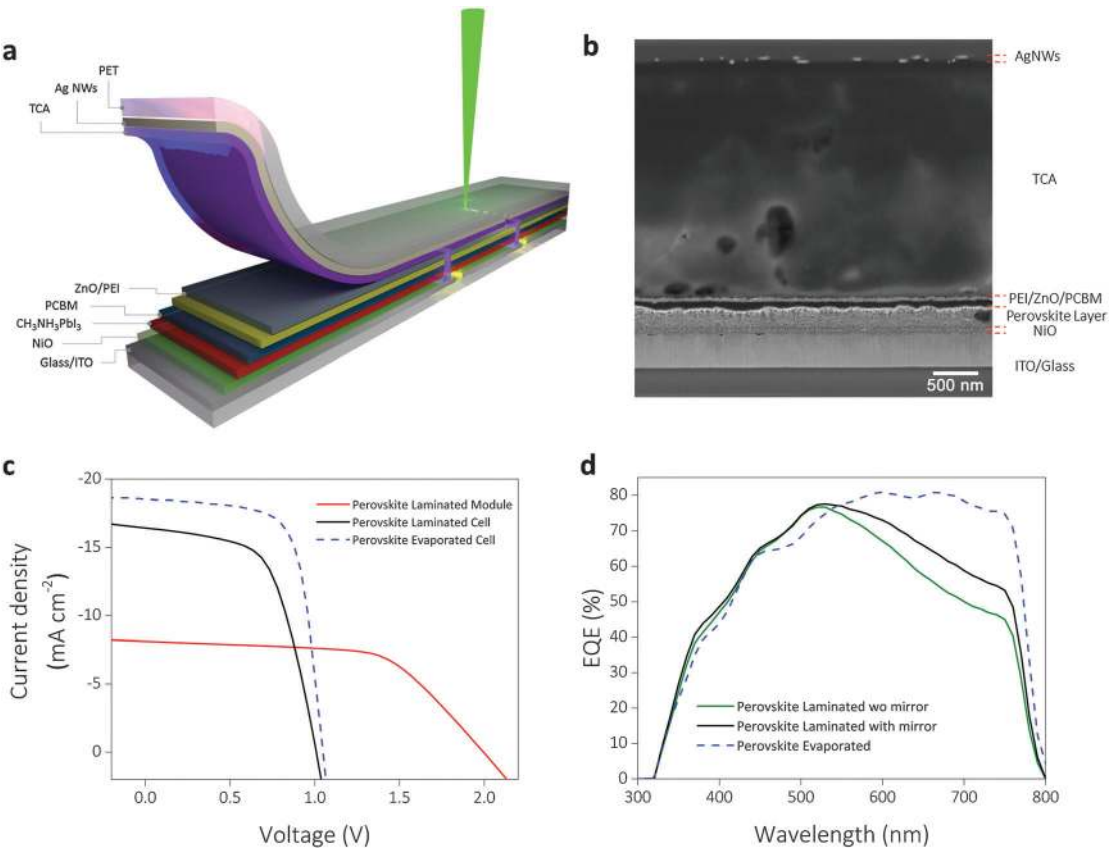

Fig. 4 (a) Device architecture of laminated perovskite solar cell/module. (b) Cross-section scanning electron microscopy image of laminated perovskite solar device on glass substrate. (c) J–V characteristics of perovskite solar cells and modules with laminated top electrode. (d) EQE spectra of reference perovskite solar cell with 100 nm evaporated Ag top electrode (blue dashed line), laminated perovskite solar cell measured with reflecting mirror in the back (black line), and laminated OPV cell measured without reflecting mirror (green line).

minimized contamination (solutions printed on different substrates ensure reduced contamination of the active layer) and vacuum free (easy, fast and inexpensive lamination) processing are the most important attributes leading to a high-quality semi-transparent electrode with the additional benefit of simultaneously acting as a protective barrier towards the environment.

Laminated perovskite solar modules

To demonstrate the universality of the proposed method we fabricated perovskite solar modules with a laminated top electrode featuring the device geometry ITO/NiO/$CH_3NH_3PbI_3$/[60]PCBM/ZnO/PEI/laminated-top-electrode. Methylammonium-halide based perovskite semiconductors are a particularly challenging example as their intrinsic sensitivity towards water prohibits top coating of water-based solutions. The photoactive perovskite layer was based on methylammonium lead iodide (see Materials and methods for details). A thin film of commercial NiO nanoparticles (Nanograde) was employed as the hole transporting layer while a thin film of ZnO nanoparticles acted as the electron-selective interfacial layer (Fig. 4a and b). The low-temperature processed NiO nanoparticles were prepared by flame spray synthesis (Materials and methods). This process produces crystalline nanoparticles with a size distribution in the range of 5–8 nm, as determined by transmission electron microscopy (Fig. S3, ESI†). This device architecture was primarily selected because hole and electron transporting layers along with the intermediate buffer layers can be processed at relatively low temperatures (140 °C). Moreover, this device geometry has been shown to effectively suppress hysteresis.[51,52] During this work, we observed that $\approx$10 nm of PEI on the top of ZnO improved the electrical contact with the TCA. A cross-section SEM image in Fig. 4b shows well-defined layers and a TCA of $\approx$3 μm. The *J–V* performances of perovskite solar cells with evaporated (ITO/NiO/$CH_3NH_3PbI_3$/[60]PCBM/ZnO/PEI/Ag, evap) and laminated contacts as well as the corresponding perovskite module are presented in Fig. 4c. Reference solar cells with a thermally evaporated silver electrode demonstrate an average efficiency of 13.56%. When transitioning to a laminated electrode the average efficiency is reduced mainly due to losses in J_{sc} and FF, while V_{oc} remains almost unchanged (Table 1). The 11% loss in J_{sc} is in agreement with previous reports and can be attributed to optical interference effects as is apparent from the EQE spectra for wavelengths $>$550 nm.[14,53] Additional losses could potentially derive from the enhanced transport resistance at the TCA interface as noticed in the case of laminated OPV devices (Fig. 3d). This interface is most likely not fully optimized, even upon improvements after adding PEI on the top of ZnO.

Perovskite modules show minor losses in efficiency ($<$1%) as compared to the corresponding laminated solar cells and deliver a PCE of 9.75%. These losses are governed by J_{sc} losses while we observe a full V_{oc} (double V_{oc} with respect to the reference device) and similar FF values. The mean values and the standard deviation of population for all perovskite devices are shown in Table 1. The *J–V* characteristics in the dark are shown in Fig. S7b (ESI†). Importantly, the roll lamination of the top electrode initially developed for organic solar cells and modules can be easily adapted to work with other thin-film photovoltaic technologies, requiring only an adjustment of the laser fluence for the ablation of the P2 line. This opens up an entirely new avenue for a cost-effective fabrication route of organic and hybrid electronic appliances.

Conclusion

The widespread technological adoption of organic and hybrid electronics hinges on the availability of suitable materials combined with cost-effective fabrication methods for large area deployment. The material approaches and device engineering methods based on roll lamination presented here address both of these concerns. A composite electrode based on ubiquitous PEDOT:PSS and D-sorbitol is combined with AgNWs to form a highly functional conductive adhesive that can be coated on plastic substrates. This enables a mechanically bendable, potentially ultra-low cost electrode with micrometer thickness that could be printed on a roll-to-roll coater and combined with various technologies, including semi-transparent devices. The composite electrode exhibits transport and recombination resistances comparable with evaporated silver. As a result, we demonstrate organic and perovskite solar cells and modules without major sacrifices in efficiency and we are confident that this concept will be of relevance to other technologies such as CIGS, a-Si:H, CZTS (copper zinc tin sulfide) or HIT (heterostructure with intrinsic thin layer) solar cells. A key technological advancement in the fabrication of thin film modules is attained through the demonstration of depth-resolved, layer selective laser patterning through the laminated device, which simultaneously grants high geometrical fill factors, a simplified fabrication protocol and a route towards inherent packaging at the earliest possible state. We envision that this lamination technology could be further extended to realize a universal process where worn-out electrodes are delaminated and reapplied, and lamination is switched between single, tandem and multilayer devices. We further anticipate that the implementation of high speed, high precision laser post-lamination patterning enhanced with 3D scribing capability will further advance future thin-film electronics.

Author contributions

G. D. S. coordinated the experiments, performed device fabrication and characterization, and designed the figures. G. D. S. and M. S. wrote the manuscript with comments from all co-authors. C. O. R. Q., Y. H. and G. D. S. fabricated the perovskite devices. N. G. and G. D. S. performed impedance characterization and analysis of the data. P. S. and E. S. contributed with the electron microscopy analysis. J. A. and G. D. S. performed the dark lock-in thermography measurements. P. K. and G. D. S. optimized the laser patterning. N. L. and M. S. assisted with data interpretation and contributed ideas. T. A., H. J. E. and C. J. B. supervised the project.

Acknowledgements

The authors gratefully acknowledge support by the Cluster of Excellence ''Engineering of Advanced Materials (EAM)'' at the University of Erlangen-Nuremberg, which is funded by the German Research Foundation (DFG) within the framework of its ''Excellence Initiative''. The authors acknowledge the Solar Factory of the Future as part of the Energy Campus Nuremberg (EnCN), which is supported by the Bavarian State Government (FKZ 20-3043.5); G. D. S. and H. J. E. acknowledge the German Federal Ministry of Education and Research (BMBF, grant no. 03EK3501 l). M. S. acknowledges primary support from a fellowship from the Portuguese Fundação para a Ciência e a Tecnologia (SFRH/BPD/71816/2010). C. O. R. Q. would like to gratefully acknowledge the financial support from The Mexican National Council for Science and Technology (CONACYT). N. L. is grateful for the financial support from the Bavarian Ministry of Economic Affairs and Media, Energy and Technology by funding the Joint Projects of the Helmholtz-Institute Erlangen-Nürnberg for Renewable Energy Production (HI-ERN).

References

1 http://www.worldenergyoutlook.org/resources/energydevelopment/energyaccessdatabase/.
2 J. Gong, S. B. Darling and F. You, *Energy Environ. Sci.*, 2015, **8**, 1953–1968.
3 A. C. Arias, J. D. MacKenzie, I. McCulloch, J. Rivnay and A. Salleo, *Chem. Rev.*, 2010, **110**, 3–24.
4 M. Kaltenbrunner, M. S. White, E. D. Głowacki, T. Sekitani, T. Someya, N. S. Sariciftci and S. Bauer, *Nat. Commun.*, 2012, **3**, 770.
5 M. Kaltenbrunner, G. Adam, E. D. Glowacki, M. Drack, R. Schwodiauer, L. Leonat, D. H. Apaydin, H. Groiss, M. C. Scharber, M. S. White, N. S. Sariciftci and S. Bauer, *Nat. Mater.*, 2015, **14**, 1032–1039.
6 M. A. Green, K. Emery, Y. Hishikawa, W. Warta and E. D. Dunlop, *Prog. Photovoltaics*, 2015, **23**, 805–812.
7 Z. He, C. Zhong, S. Su, M. Xu, H. Wu and Y. Cao, *Nat. Photonics*, 2012, **6**, 591–595.
8 N. J. Jeon, J. H. Noh, W. S. Yang, Y. C. Kim, S. Ryu, J. Seo and S. I. Seok, *Nature*, 2015, **517**, 476–480.
9 M. C. Scharber, *Adv. Mater.*, 2016, **28**, 1994–2001.
10 S. R. Forrest, *Nature*, 2004, **428**, 911–918.
11 F. Machui, M. Hosel, N. Li, G. D. Spyropoulos, T. Ameri, R. R. Sondergaard, M. Jorgensen, A. Scheel, D. Gaiser, K. Kreul, D. Lenssen, M. Legros, N. Lemaitre, M. Vilkman, M. Valimaki, S. Nordman, C. J. Brabec and F. C. Krebs, *Energy Environ. Sci.*, 2014, **7**, 2792–2802.
12 R. Søndergaard, M. Hösel, D. Angmo, T. T. Larsen-Olsen and F. C. Krebs, *Mater. Today*, 2012, **15**, 36–49.
13 F. Guo, X. Zhu, K. Forberich, J. Krantz, T. Stubhan, M. Salinas, M. Halik, S. Spallek, B. Butz, E. Spiecker, T. Ameri, N. Li, P. Kubis, D. M. Guldi, G. J. Matt and C. J. Brabec, *Adv. Energy Mater.*, 2013, **3**, 1062–1067.
14 C. O. Ramírez Quiroz, I. Levchuk, C. Bronnbauer, M. Salvador, K. Forberich, T. Heumüller, Y. Hou, P. Schweizer, E. Spiecker and C. J. Brabec, *J. Mater. Chem. A*, 2015, **3**, 24071–24081.
15 C.-C. Chen, L. Dou, R. Zhu, C.-H. Chung, T.-B. Song, Y. B. Zheng, S. Hawks, G. Li, P. S. Weiss and Y. Yang, *ACS Nano*, 2012, **6**, 7185–7190.
16 E. Kymakis, K. Savva, M. M. Stylianakis, C. Fotakis and E. Stratakis, *Adv. Funct. Mater.*, 2013, **23**, 2742–2749.
17 M. P. Ramuz, M. Vosgueritchian, P. Wei, C. Wang, Y. Gao, Y. Wu, Y. Chen and Z. Bao, *ACS Nano*, 2012, **6**, 10384–10395.
18 H. Kang, S. Jung, S. Jeong, G. Kim and K. Lee, *Nat. Commun.*, 2015, **6**, 6503.
19 T. M. Eggenhuisen, Y. Galagan, A. F. K. V. Biezemans, T. M. W. L. Slaats, W. P. Voorthuijzen, S. Kommeren, S. Shanmugam, J. P. Teunissen, A. Hadipour, W. J. H. Verhees, S. C. Veenstra, M. J. J. Coenen, J. Gilot, R. Andriessen and W. A. Groen, *J. Mater. Chem. A*, 2015, **3**, 7255–7262.
20 M. Granstrom, K. Petritsch, A. C. Arias, A. Lux, M. R. Andersson and R. H. Friend, *Nature*, 1998, **395**, 257–260.
21 A. Tada, Y. Geng, Q. Wei, K. Hashimoto and K. Tajima, *Nat. Mater.*, 2011, **10**, 450–455.
22 J. Ouyang and Y. Yang, *Adv. Mater.*, 2006, **18**, 2141–2144.
23 J. Huang, G. Li and Y. Yang, *Adv. Mater.*, 2008, **20**, 415–419.
24 J.-Y. Lee, S. T. Connor, Y. Cui and P. Peumans, *Nano Lett.*, 2010, **10**, 1276–1279.
25 J.-H. Huang, Z.-Y. Ho, T.-H. Kuo, D. Kekuda, C.-W. Chu and K.-C. Ho, *J. Mater. Chem.*, 2009, **19**, 4077–4080.
26 R. Steim, P. Chabrecek, U. Sonderegger, B. Kindle-Hasse, W. Siefert, T. Kroyer, P. Reinecke, T. Lanz, T. Geiger, R. Hany and F. Nüesch, *Appl. Phys. Lett.*, 2015, **106**, 193301.
27 B. A. Bailey, M. O. Reese, D. C. Olson, S. E. Shaheen and N. Kopidakis, *Org. Electron.*, 2011, **12**, 108–112.
28 Y. Yuan, Y. Bi and J. Huang, *Appl. Phys. Lett.*, 2011, **98**, 063306.
29 C. Shimada and S. Shiratori, *ACS Appl. Mater. Interfaces*, 2013, **5**, 11087–11092.
30 D. Kaduwal, B. Zimmermann and U. Würfel, *Sol. Energy Mater. Sol. Cells*, 2014, **120**(Part B), 449–453.
31 D. Bryant, P. Greenwood, J. Troughton, M. Wijdekop, M. Carnie, M. Davies, K. Wojciechowski, H. J. Snaith, T. Watson and D. Worsley, *Adv. Mater.*, 2014, **26**, 7499–7504.
32 J. H. Heo, H. J. Han, M. Lee, M. Song, D. H. Kim and S. H. Im, *Energy Environ. Sci.*, 2015, **8**, 2922–2927.
33 M. Nakamura, C. Yang, E. Zhou, K. Tajima and K. Hashimoto, *ACS Appl. Mater. Interfaces*, 2009, **1**, 2703–2706.
34 A. R. B. M. Yusoff, S. J. Lee, F. K. Shneider, W. J. da Silva and J. Jang, *Adv. Energy Mater.*, 2014, **4**, 1301989.
35 V. C. Tung, J. Kim, L. J. Cote and J. Huang, *J. Am. Chem. Soc.*, 2011, **133**, 9262–9265.
36 J. H. Heo and S. H. Im, *Adv. Mater.*, 2015, DOI: 10.1002/adma.201501629.
37 G. D. Spyropoulos, P. Kubis, N. Li, D. Baran, L. Lucera, M. Salvador, T. Ameri, M. M. Voigt, F. C. Krebs and C. J. Brabec, *Energy Environ. Sci.*, 2014, **7**, 3284–3290.
38 S. Berny, N. Blouin, A. Distler, H.-J. Egelhaaf, M. Krompiec, A. Lohr, O. R. Lozman, G. E. Morse, L. Nanson, A. Pron, T. Sauermann, N. Seidler, S. Tierney, P. Tiwana, M. Wagner

and H. Wilson, *Adv. Sci.*, 2016, **3**, DOI: 10.1002/advs.201500342.

39 L. Lucera, F. Machui, P. Kubis, H. D. Schmidt, J. Adams, S. Strohm, T. Ahmad, K. Forberich, H. J. Egelhaaf and C. J. Brabec, *Energy Environ. Sci.*, 2016, **9**, 89–94.

40 P. Kubis, N. Li, T. Stubhan, F. Machui, G. J. Matt, M. M. Voigt and C. J. Brabec, *Prog. Photovoltaics*, 2015, **23**, 238–246.

41 J. Bachmann, C. Buerhop-Lutz, C. Deibel, I. Riedel, H. Hoppe, C. J. Brabec and V. Dyakonov, *Sol. Energy Mater. Sol. Cells*, 2010, **94**, 642–647.

42 A. Helbig, T. Kirchartz, R. Schaeffler, J. H. Werner and U. Rau, *Sol. Energy Mater. Sol. Cells*, 2010, **94**, 979–984.

43 B. J. Leever, C. A. Bailey, T. J. Marks, M. C. Hersam and M. F. Durstock, *Adv. Energy Mater.*, 2012, **2**, 120–128.

44 A. Guerrero, T. Ripolles-Sanchis, P. P. Boix and G. Garcia-Belmonte, *Org. Electron.*, 2012, **13**, 2326–2332.

45 F. Fabregat-Santiago, G. Garcia-Belmonte, I. Mora-Sero and J. Bisquert, *Phys. Chem. Chem. Phys.*, 2011, **13**, 9083–9118.

46 N. Gasparini, S. Righi, F. Tinti, A. Savoini, A. Cominetti, R. Po and N. Camaioni, *ACS Appl. Mater. Interfaces*, 2014, **6**, 21416–21425.

47 H. Zhou, Y. Zhang, J. Seifter, S. D. Collins, C. Luo, G. C. Bazan, T.-Q. Nguyen and A. J. Heeger, *Adv. Mater.*, 2013, **25**, 1646–1652.

48 S. Hoshino, M. Yoshida, S. Uemura, T. Kodzasa, N. Takada, T. Kamata and K. Yase, *J. Appl. Phys.*, 2004, **95**, 5088–5093.

49 M. S. A. Abdou, F. P. Orfino, Y. Son and S. Holdcroft, *J. Am. Chem. Soc.*, 1997, **119**, 4518–4524.

50 Y. Suh, N. Lu, S. H. Lee, W.-S. Chung, K. Kim, B. Kim, M. J. Ko and M. J. Kim, *ACS Appl. Mater. Interfaces*, 2012, **4**, 5118–5124.

51 J. Xiong, B. Yang, R. Wu, C. Cao, Y. Huang, C. Liu, Z. Hu, H. Huang, Y. Gao and J. Yang, *Org. Electron.*, 2015, **24**, 106–112.

52 Y. Shao, Z. Xiao, C. Bi, Y. Yuan and J. Huang, *Nat. Commun.*, 2014, **5**, 5784.

53 Q. Lin, A. Armin, R. C. R. Nagiri, P. L. Burn and P. Meredith, *Nat. Photonics*, 2015, **9**, 106–112.